Available online at www.HEFJournal.org

ISSN: 2785-2997

Journal of
Human, Earth, and Future

Vol. 5, No. 4, December, 2024

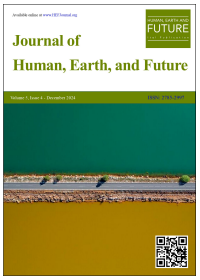

Technique for Segmentation and Selection of Biomedical Images

Vladimir Zh. Kuklin [1*], Leonid M. Chervyakov [1], Andrei N. Ruslantsev [1], Tagirbek G. Aslanov [1]

[1] *Institute of Design and Technology Informatics, Russian Academy of Sciences, Russian Federation.*

Received 20 September 2024; Revised 14 November 2024; Accepted 21 November 2024; Published 01 December 2024

Abstract

Various research fields, such as biology and medicine, have increasingly used techniques for the machine estimation of generated pulses. For example, in biological medicine, classifying information makes it possible to automate the interpretation of incoming data obtained owing to diagnosis, which is necessary when processing large volumes of information arrays. This study aims to develop algorithms that enable the selection of single-type objects in images with subsequent image splitting into a set list of segments with heterogeneous tension, even when the number of reference images is very small. Analysis of existing algorithms allowed us to determine the focus area for developing and improving the efficiency of the algorithms. The existing algorithms show poor performance results in analyzing the dark parts of images, so it makes sense to develop an algorithm for image intensity normalization. The developed algorithm simplifies the procedure of partitioning the training base for the classifier owing to the use of the feature vectors. A random forest algorithm was used for image classification, followed by boundary refinement using a Markov field. The image-splitting algorithm precisely separates parts of the brain structure by applying a Markov field to refine classification results. The proposed classification algorithm showed strong results in comparison with existing algorithms, particularly in the comparison of the Dice criterion. The proposed method shows an average increase of 10% in classification accuracy. One way to improve the presented algorithm is to add texture elements to the feature vector, which allows the identification of distinguishing features of the elements, such as shape and length, which could improve this algorithm for a more accurate classification of substructures.

Keywords: Image Segmentation; Image Splitting; Medical Biology; Brain Structure; Tension.

1. Introduction

Scientific studies, including biological and medical experiments, are increasingly using machine pulse estimation techniques. Currently, methods are available to classify medical information, making it possible to identify objects in images. In medical biology, these methods automate the process of interpreting information resulting from diagnostics that are in great demand when processing large information arrays and visual estimation of the obtained data. The almost continuous increase in the volume of calculations and their automation are the main factors contributing to the development of more accurate calculation methods and accelerated information processing.

The available equipment makes it possible to obtain high-quality images depicting almost any internal organ through a series of multidimensional images or a chain of characteristic segments in 2D planes. In processing the obtained images, difficulties sometimes arise in semantic segmentation, that is, separating objects corresponding to a

* Corresponding author: kuklin_vladimir_ran@mail.ru

http://dx.doi.org/10. 28991/HEF-2024-05-04-011

defined group. These difficulties can also complicate image segmentation into several anatomical components and reveal particular pathologies [1].

When segmenting an image describing a particular body fragment into several anatomical components, professionals often use atlases that contain images of standard body fragments with clear anatomical markings. However, in practice, it is essential to consider the specificity of the studied organism to transfer markings more accurately.

Most available techniques for processing objects in medical images rely on machine-learning processes. Machine learning is a set of algorithmic techniques that allows computer systems to make data-driven predictions from large datasets. These techniques have various applications that can be tailored to the medical field. Significant efforts have been made to develop classical machine-learning algorithms for the segmentation of normal (e.g., white matter and gray matter) and abnormal brain tissues. However, the creation of imaging features that enable such segmentation requires careful engineering and expertise. Furthermore, traditional machine-learning algorithms do not generalize well. Despite significant efforts from the medical imaging research community, automated segmentation of brain structures and detection of abnormalities remain unsolved problems because of normal anatomical variations in brain morphology, image acquisition imperfections, and variations in the appearance of pathology [2].

During pathological identification, the main difficulties arise with imitation. Most atlases usually involve internal organs in a normal state. However, different pathologies have different parameters, complicating their identification by clarifying their shape, degree of activity, and current location. In addition, in some cases, it is impossible to obtain significant information arrays, or the process of obtaining such arrays is complicated [3]. Therefore, we propose an iterative biomedical image classification algorithm based on classification using a randomized solver forest by applying a Markov field to refine the resulting segmentation.

2. Literature Review

Today, many available practical techniques provide images of human organs, divided into invasive and non-invasive techniques, with a certain degree of conditionality. The first category includes methods for obtaining images using histology. The second category covers techniques that do not involve direct invasion of the human body. This category covers ultrasound techniques, magnetic resonance imaging (MRI), and computed tomography (CT).

MRI offers high-quality images that are clearer than CT; therefore, this technique is more often used to diagnose pathologies of the brain of the central nervous system. As a rule, MRI images preserve the data obtained during the study using a sequence of 2D images with some periodicity [4, 5].

A classic histological section is a lancet cut in a particular area, which is necessary to obtain an image. This technique uses dyes that outline the contours of the cells in question, their structures, and others. As a rule, these studies used several types of dye [6].

Image series transfer to information arrays. Conversion and storage of this information follow protocols that standardize the procedures of information exchange in the community of specialized professionals. After studying images, the professional can mark detected pathologies or areas that contain other important information [7].

Medical practice increasingly uses image-processing algorithms, which automate and reduce the time required for such procedures. Computer-aided diagnostics (CAD) also uses these algorithms. In addition, using these algorithms opens broad prospects for diagnostics and the application of more effective therapy [8, 9].

The first-generation techniques are simple but specific and cannot serve as the main ones. Their weaknesses include high sensitivity to noise components, uneven illumination, and different tensions of the studied objects. The considered techniques can only solve narrowly focused tasks, such as evaluating pathologies, contrasting with normal tissue, or pathologies outlined with sharp contours. However, this group of techniques applies in combination with other more advanced techniques [10, 11]. Second-generation techniques rely on mathematical calculations; however, they also have disadvantages. The methods based on the splitting of significant points of the considered object in the image operate mainly with the tension of these points, whose capacity does not always make it possible to reliably distribute the significant points and surrounding background [12].

The effectiveness of these techniques is largely determined by the established approximation that detects foci on strictly defined fragments. In addition, their effectiveness relies on processing a relatively small number of characteristics [13-15].

Most available techniques do not consider the preliminary data of an image used as a reference. When registering significant points based on their multidimensional displacements, comparing test images with reference ones (simply speaking, with images from atlases) must also be trained by 3-5 cases to identify the list of probable displacements.

V-Net is a network modified from U-Net and was first proposed specifically for medical image analysis. Although it demonstrated good segmentation performance on prostate MR images, it did not perform well in our fetal MRI tissue segmentation, where it completely failed in segmentation tasks of the cerebellum, deep grey matter, and brainstem. A possible reason was that it did not make full use of the global context information of various tissue structures, so it was not strong enough for feature extraction. DMFNet, relative to V-Net, was able to segment the above three brain tissues better because the 3D-dilated convolution introduced in DMFNet can build multiscale feature representations and help extract smaller tissue patches, which were also used in our network. However, it has too many parameters and is too long to run for quick diagnosis. Moreover, a major feature of medical images is the small amount of available data. Therefore, if the network structure is too complex and there are too many parameters, the trained model may suffer from overfitting and bias [16].

For computational methods, extraction of the most relevant and important features is a key task, and if performed manually, it may lead to degraded performance, where feature engineering experts can easily miss the relevant features. Neural-network-based methods can extract useful features automatically, and the number of such features can range from dozens to billions, which is impossible in manual engineering. Artificial intelligence can be effectively used for the detection, segmentation, and classification of multiple diseases. Regarding the problems of this method, its reproducibility in clinical settings should be interpreted with caution. This study was based on a specific dataset and model, and it may not be possible to replicate the results obtained on a different dataset or using a different model. In addition, the availability of similar data and resources in clinical settings may be limited [17].

There are different ways to improve segmentation methods, one of which is EG-TransUNet, which is an adaptation of U-Net. Using the transformer can deepen the decoding process of high-level semantic features, and low-level texture features can be combined to gradually improve the edge part. In addition, the resolution of the decoded image was gradually improved, and the details of the image were gradually enriched, making the decoded image closer to the real result [18].

However, in our study, we focused on the application of the Markov field to improve the quality of segmentation. For example, there is a goal-driven unsupervised image segmentation method that, thanks to a novel definition of image segmentation taking into consideration a user-defined goal, is capable of partitioning the input image into a set of homogeneous regions of interest and a background area. By combining weighted graphs, parametric density modeling, and Markov random field modeling, the proposed method has been experimentally demonstrated to be effective in two different domains of applicability: medical magnetic resonance images and remote-sensing SAR imagery [19].

Deep learning is capable of learning high-level feature representations automatically and has emerged as a powerful mechanism in automated volumetric medical image segmentation. Moreover, engrafting statistical methodologies in deep networks improves biomedical image segmentation. Thus, volumetric 3D MRI segmentation at the intersection of statistical modeling and deep learning can be considered a more effective alternative to methods that are purely statistical or deep learning-based. Medical image segmentation encompasses a broad set of challenges, including complex and subtle surrounding boundaries of organs, lack of sufficient level of region uniformity and similarity, low contrast and intensity inhomogeneity, image noise, partial volume effect, and other artifacts that impede the precise identification of abrupt variations between organs of interest [20].

3. Objects and Methods of Research

The main essence of the image-splitting technique is to create contour lines of tension, among which there is a group of contour lines of the studied objects. These contour lines are selected using multiclass codifiers to exclusively analyze closed contour lines. The control points of these codifiers are several shaping parameters of the object described by the contour line and the tension characteristics of the image fragment of the contour line location. Contour lines of tension dependence are drawn using a contouring technique. The contour lines representing the outlines of the considered objects were selected by a codifier operating with base gradients. Figure 1 presents a flowchart of the overall structure of the presented work.

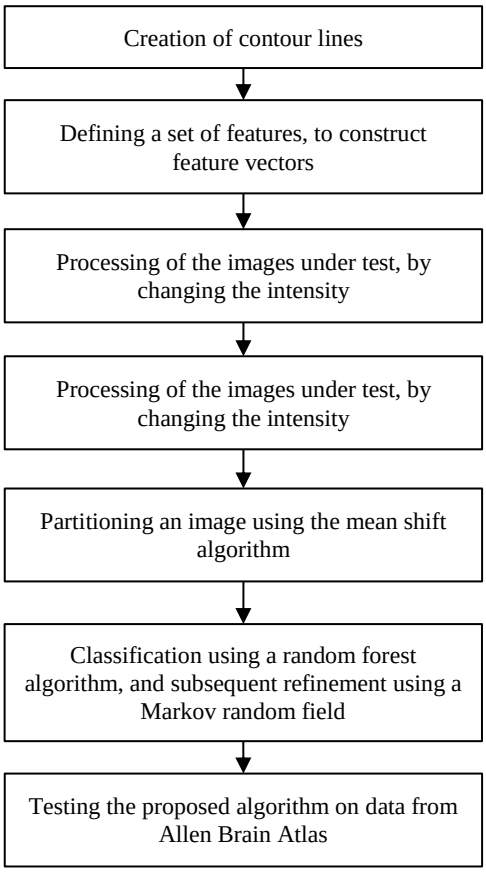

Figure 1. Workflow flowchart

To increase the reliability of the final result provided by this technique, it functions in semi-automatic mode. As a rule, a professional marks several rectangular fragments on the images of an object's location (Figure 2a). The objects were then machine marked in the outline of the marked fragments (Figure 2b). This method is similar to the "weak-tag technique.

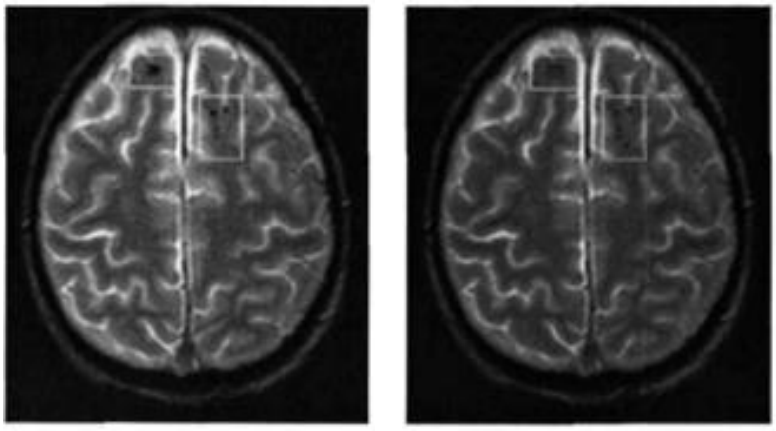

(a) (b)

Figure 2. Image of object separation in semi-automatic mode: a) – selection of the interesting rectangular area of the image by a specialist; b) – machine marking inside the interesting rectangular area

Contour line drawing techniques are typically applied to develop a contour line map represented by the dependence of the variation of the two main arguments. The contour line of the dependence $f(x,y)$ represents the specific location of the arguments (x,y) when $f(x,y)$ = const. The contour line h of the dependence $f(x,y)$ represents the location of the arguments (x,y) when $f(x,y) = h$. When h belongs to the spectrum of values of dependence $f(x,y)$, there can be a single or a limited number of contour lines concerning h. Drawing contour lines aims to create geographic (other specialized) maps used in geology, meteorology, etc.

Many studies have described and proposed contour line-drawing techniques. We relied on the contour plot technique in MATLAB. Here, the dependence $f(x,y)$ is expressed by the intensity of the point $I(x, y)$, i.e., the map drawn for the image determines coordinate heights (x,y) by the tension of point (x,y) on the initial image, then using the technique for drawing contour lines for the position h or the set tension value [21].

The image resembled a multidimensional grid. The extreme points of this grid correspond to the tensions of the significant points, and the edges connect neighboring points (Figure 3). Examining all the grid quadrilaterals individually, the middle quadrilateral, the beginning of contour line h, is selected on the grid. Subsequently, extreme points a_i and a_j, located on the edge are controlled by the expression;

$$(f(a_i) - h) * (f(a_j) - h) \leq 0 \quad (1)$$

If the calculated value corresponds to the expression, the tension of the extreme points of the edge exceeds h, the tension of the opposite extreme points of the edge will be lower than the current h. It turns out that the considered contour line h belongs to the quadrilateral or its edge:

$$t = \frac{h - f(a_i)}{f(a_j) - f(a_i)} \quad (2)$$

$$hx(k) = a_i(x) + t * \left(a_j(x) - a_i(x)\right) \quad (3)$$

$$hy(k) = a_i(y) + t * \left(a_j(y) - a_i(y)\right) \quad (4)$$

Here, a_i represents the extreme point characterized by a lower tension value, k is the index of the current values of the contour line under consideration (considering $k = 1$).

Next, the quadrilateral adjacent to the edge crossed by the contour line was considered, marking the previous quadrilateral as checked. The next quadrilateral is considered by exiting the edges using expression (1). Expressions (2-4) calculate the spatial location of key points for each edge intersected by the contour line to send the result to a particular cluster. Recording in a cluster occurs until the contour lines are

- Cross the initial quadrilateral;
- Enter the previously checked quadrilateral;
- Leave the limits of the considered image fragment.

Next, the current k sets to zero, selecting new contour lines h. Figure 3 shows the practical drawing of contour lines. Here, the quadrilaterals of white color with dark edges are analogous to the significant points.

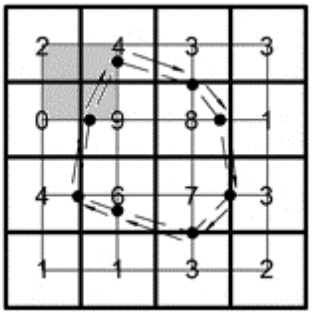

Figure 3. Appearance of contour lines drawing at h = 5

The selected contour lines necessary to separate the objects in the images were closed. In the third variant, the contour line is not closed because it crosses the image area under consideration. Figure 4 shows the contour line drawing of the fragment marked by a professional. The figure shows a definite list of layers for which the closed contour lines are identical to the outlines of the objects under consideration.

To separate the closed contour lines describing the outline of objects from other closed lines, a list of characteristics is necessary. As a rule, manual separation makes it possible to identify the required lines by simply separating the characteristics similar to those typically used by a professional when estimating the considered image fragment.

In general, there are several characteristics, such as:

- Length and width of the fragment under study;
- Compactness of neighboring contour lines;
- Distance between significant lines.

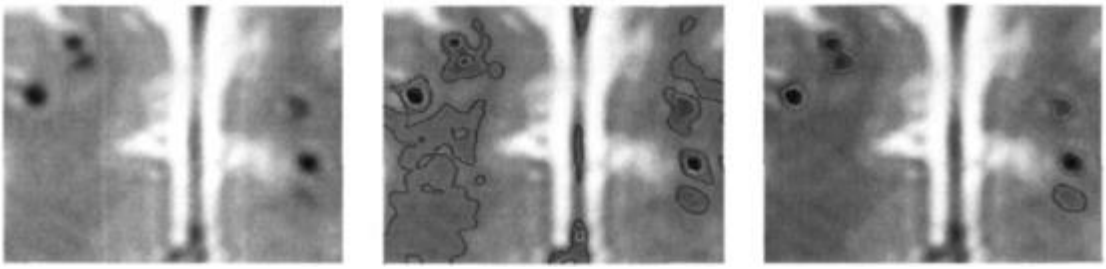

Figure 4. Appearance of contour lines of the considered image fragment

The characteristics of the considered image fragment with the contour line depend on the tension; in particular, it is of interest:

- The difference in tension along the outline of the closed contour line;
- Ratio of the averaged tension of a closed contour line to that of a quadrilateral fragment.

The basic gradient technique is often applied to machine learning, as detailed in [22]. Creating a multidimensional plane is an effective classification method [23].

Suppose we have a training selection with n components represented by gradient characteristics $x_i \in R^r$ corresponding to group $y_i \in \{-1, +1\}$:

$$X^n = \{(x_i, y_i): i = 1,2,\dots, n\} \tag{5}$$

It is necessary to calculate the dependence $f: R^r \to R$, which fully describes the work of the sorter.

$$C(x) = sign\big(f(x)\big) \tag{6}$$

Considering the elementary case when $y_i = +1$ and $y_i = -1$are values from selection X_n, we have:

$$\{x: f(x) = wx + b = 0\} \tag{7}$$

Here, w is the mass gradient; b is the current displacement.

Then we can use w and b, so;

$$wx_i + b \geq +1, \text{ , when } y_i = +1 \tag{8}$$

$$wx_i + b \leq -1, \text{ , when } y_i = -1 \tag{9}$$

The gradients of selection X^n corresponding to expression (8) are part of the multidimensional plane $H_{+1}: wx + (b - 1) = 0$. Consequently, gradients X^n corresponding to (9) are part of the multidimensional plane $H_{-1}: wx + (b + 1) = 0$. The gradients that are part of multidimensional planes H_{-1} or H_{+1} are commonly called base gradients (Figure 5). We can calculate the distance separating the neighboring multidimensional planes described by expression (7).

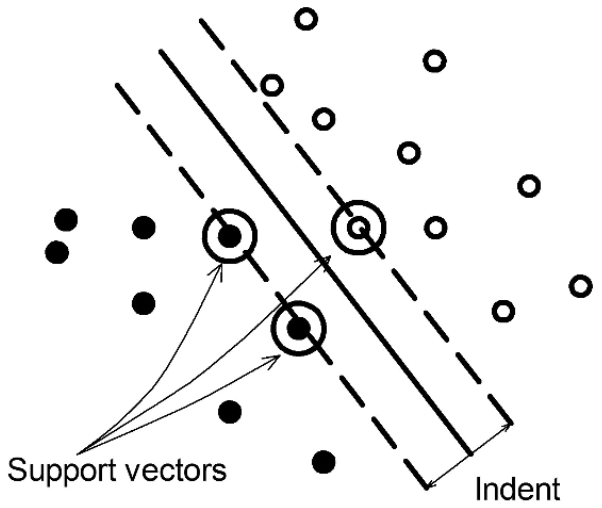

Figure 5. Set of key points separated by a multidimensional plane

For base gradients, the expression $wx_i + b = \pm 1$ is valid; therefore, the distance from any base gradient to a multidimensional plane is $\frac{1}{\|w\|}$. The distance separating the neighboring multidimensional planes H_{+1} and H_{-1} corresponds to $\frac{2}{\|w\|}$. We calculated the indentation between the significant points divided by a multidimensional plane.

Let us transform relations (8-9) into:

$$y_i(wx_i + b) \geq 1, i = 1,2,\ldots,n \tag{11}$$

Therefore, we need:

to reduce $\frac{1}{2}ww^T$ (12)

when $y_i(wx_i + b) \geq 1$ (13)

For that:

$$F(b,w,\alpha) = \frac{1}{2}\|w\|^2 - \sum_{i=1}^{n} \alpha_i\{y_i(wx_i + b) - 1\} \tag{14}$$

$$\alpha = (\alpha_1,\ldots,\alpha_n) \geq 0 \tag{15}$$

We should calculate the smallest values for currents *b* and *w*, while for min *F*, it is necessary to calculate the maximum values of α.

Therefore,

$$w = \sum_{i=1}^{n} \alpha_i y_i x_i \tag{16}$$

$b = y_i - x_i w$ for any base gradients (17)

Masses α_i will not correspond to zero values of the base gradients; therefore, solely the base gradients will determine the spatial location of the multidimensional plane. Using the current *w* in dependence *f*(*x*) from expression (7), we have;

$$f(x) = wx + b = \sum_{i=1}^{n} \alpha_i y_i x_i x + b \tag{18}$$

Therefore, we obtain the class marking with respect to any gradient *x* when sign(*f*(*x*)).

The generated technique describes the summary of gradient characteristics obtained in training selections where the considered dependence is divisible (Figure 6). This problem (12-13) can be solved by multiplying the pairs of gradients from the collection [24].

Therefore, let us replace expression $\phi(x)$ with kernel dependence *K*:

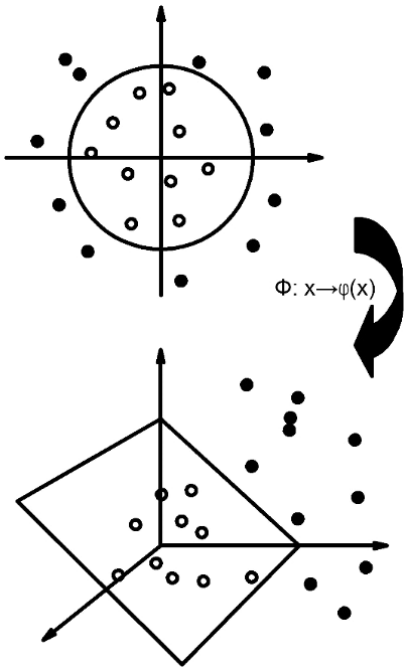

Figure 6. Mapping the initial feature space to a multidimensional space, in which the training sample becomes linearly separable

Appearance of the initial characteristics superimposed by a linear law is as follows:

$$K(x_i, x_j) = \phi(x_i)\phi(x_j) \tag{19}$$

Let us use the kernel to build a new dependency:

$$f(x) = \sum_{i=1}^{n} \alpha_i y_i K(x_i, x) + b \tag{20}$$

Applying activation function *K* using base dependence (RBF), we obtain

$$K(x, y) = exp\left\{-\frac{\|x-y\|^2}{2\sigma^2}\right\} \tag{21}$$

Only one characteristic σ describes the dependence. Therefore, we used the following base-gradient technique:

$$K(\mathrm{x,y}) = \langle\langle x, y\rangle + c\rangle^d \tag{22}$$

Here, two characteristics – *c* and *d* describe this dependence. The base-gradient technique has several advantages. It selects the correct solution groups based on the optimal transformation of the convex dependencies. Thus, we eliminate the possibility that the sought gradients correspond to minima, in contrast to neural-network sorters and decision trees. In addition, the technique increases the indentation among neighboring classes, improving the sorter's ability to generalize, that is, it becomes possible to classify items that are not in the primary selection. The technique also exhibited a good performance.

For training the sorter, it is necessary to generate training selections (5) covering all closed contour lines, including "objects" or "environment of objects," characterizing these contour lines. Any contour line corresponds to the gradient x_i. Meanwhile, the value $y_i$will is 1 when fixing the "object" and -1 for the "object environment."

Therefore, to build the sorter, the RBF base gradient technique was used (21). It showed better performance than Eq. (22). Thus, we do not rely on a single kernel but use their linear combination [25]. After completing sorter creation, we use dependency (20) to derive the grade marker for any new gradient characteristic *x*.

To mark the outlines of the considered fragments, let us:

- Build contour lines concerning the same spectrum of layers previously involved in training selection.
- Select only closed contour lines from the created contour lines;
- Calculate the gradient-characteristic for any closed line;
- Use the previously created sorter for all gradients as characteristics;
- Leave only several closed contour lines to which the sorter unambiguously points, perceiving them as an "object."

Therefore, in any significant quadrilateral fragment, it is possible to create final images with outlines of the studied objects using this technique.

We describe the created technique of image splitting into a set list of segments. This can function in one training case. The image with the applied marking lines was the test image. The image used to train the technique is called a reference or training image. This technique operates based on the hypothesis that both images have an identical list of fragments, and their outlines may not change significantly, as shown in Figure 7.

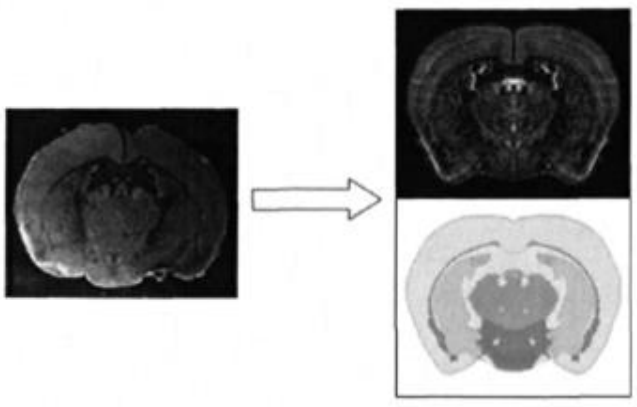

Figure 7. Appearance of the test image as well as taken from the atlas

The stochastic decision forest acts as a sorter. We used the mean shift technique to split the image into a particular list of significant points. Medical images have inherently unequal light exposure, which makes further ordered splitting difficult. Light exposure smoothing is one stage of the technique used to recreate uniform light exposure in the test image. A reference image is usually taken from atlases (where all images have the same light exposure). Figure 8 shows the light-exposure smoothing process, where;

a) The unprocessed test image;

b) The image impression;

c) The result of the Retinex technique;

d) Correction of the image beyond the impression;

f) The technique used for smoothing light exposure.

Retinex is a well-known technique that effectively smooths light exposure. Here, the image $Z(x,y)$ is expressed by the relation $Z(x,y) = R(x,y)I(x,y)$ of the considered image $R(x,y)$ and the discontinuous dependence of light exposure $I(x,y)$. Since there are no refined data on the dependence describing light exposure $I(x,y)$, let us estimate it by comparison with the considered image: $I(x,y) = G(Z(x,y))$ [26].

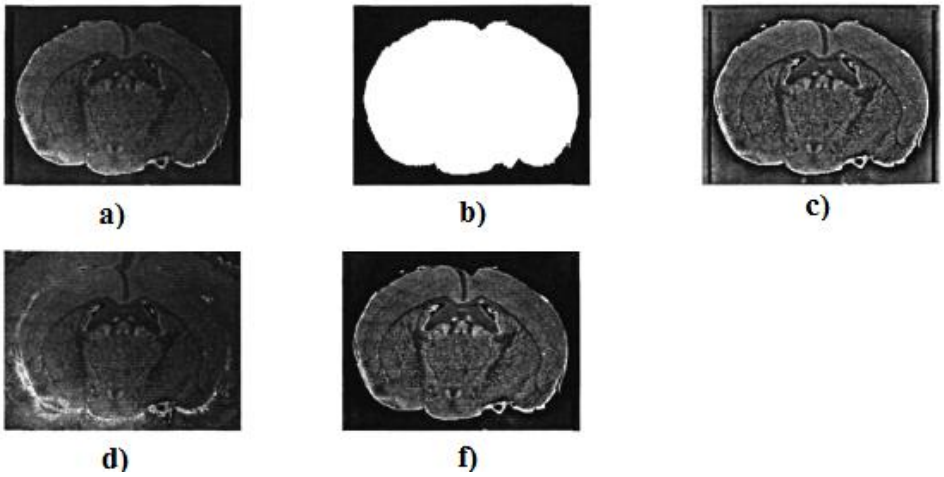

Figure 8. Appearance of the light exposure smoothing process: a) – unprocessed test image; b) – image cast; c)– result of the Retinex method; d) – correction of the image outside the cast; f) – applied method of smoothing the light exposure

Obtaining a somewhat blurred image is the result of the convolution of kernel $G(x,y)$:

$$G(x,y;\sigma) = \frac{1}{2\pi\sigma^2} e^{-\frac{x^2+y^2}{2\sigma^2}} \quad (23)$$

Here, x is the distance from its midpoint on the horizon, y is the distance from its midpoint on the vertical axis, and σ represents the error resulting from the splitting process proposed by Gauss. We applied the base values of this splitting to create a quadrilateral table describing the convolution. The center of the quadrilateral here will be $x=y=0$, while in other parts, we will get $x=y$. Let us calculate the components of the table using relation (23). In this case, each significant point of the image corresponds to a new tension value calculated by summing the tensions of the neighboring significant points:

$$I(k,l) = \sum_{k,l} f(x-k, y-l)h(k,l) \quad (24)$$

Here, $h(k,l)$ is the value of the indexed component (k,l) in the table.

Therefore, let us calculate $R(x,y)$ using $R(x,y) = \frac{Z(x,y)}{G(Z(x,y))}$.

The use of the retinex technique for processing medical images can cause several difficulties (Figure 8c). Since the light exposure difference is not far from the outlines of the considered object on the image, the use of blurring does not make it possible to fully analyze the light exposure of significant points describing the object close to its outlines; therefore, we obtain light outlines of fragments close to the outlines of the objects themselves. In addition, Retinex can form a glow close to the sharper outlines in the inner part of the object in the image.

To overcome the first difficulty, blurs G apply only to the inner part of the object outlined in the image (Figure 8b). The outline detection procedure uses the "EDISON" technique. The filtering process proceeds directly, because the

basic kernel proposed by Gauss is in the inner part of the outline. However, more efficient methods are required for this purpose. For example, it is possible to zoom in on an object outside the outline using circular reflections (Figure 8d) of the object. In such a case, $E(x,y)$ can use accelerated filtering to process the quadrilateral fragment [27].

Thus, this technique of light-exposure smoothing uses an averaged filtering cascade M as a nonlinear kernel. Similarly, the Retinex technique applies several averaged filtering cascades with different scales, expressed as $M_1M_2M_3$. The final relation for smoothing the light exposure of the enlarged object in the image can be expressed as follows:

$$R(x,y) = \frac{E(x,y)}{M(E(x,y))+\varepsilon} \tag{25}$$

$$M(x,y) = \frac{1}{3}\sum_{i=1}^{3} M_i(E_i(x,y)) \tag{26}$$

Here, E – is the energy, and ε minimizes excessive amplification of the noise component in fragments where light exposure is insufficient.

The final stage of the light-exposure smoothing technique balances the image bar diagram (the "auto-levels" procedure) shown in Figure 8e.

In contrast to the analysis of multimodal information, in our case, we operate with only one image for each case; therefore, any significant point will have several characteristics: its location in the image (x, y) and its tension value. However, as a rule, this information is insufficient to determine whether this significant point corresponds to a particular fragment. The reason for this is that, within the considered fragments, there may be considerable tension differences among neighboring significant points, which are a list united by the presence of specific qualities that distinguish this list from neighboring significant points. Because at the moment of moving from one fragment to another, the base qualities of the outline itself change, and the outlines of the considered fragments in the image are likely to correspond to the outlines of the adjacent significant points [28].

The mean shift technique, which selects the maximum values obtained in a probability distribution without simulation, is interesting. Splitting the information list into sectors occurs such that groups of points tending to the maximum value in a given fragment correspond to a single sector [29].

Initially, the information will be averaged by the filtering cascade h:

$$f(x) = \sum_i K(x - x_i) = \sum_i k\left(\frac{\|x-x_i\|^2}{h^2}\right) \tag{27}$$

Here, x_i are the initial points and $k(r)$ represents the kernel dependence.

Subsequently, the selection of the maximum local values was performed. It starts with approximation y_k, which may correspond to the initial significant pixel x_i, followed by the calculation of the dependency vector $f(x)$ and its computation:

$$\nabla f = \sum_i (x_i - x)G(x - x_i) = [\sum_i G(x - x_i)]m(x) \tag{28}$$

Here, $G = -K'$, and $m(x)$ is the mean shift gradient:

$$m(x) = \frac{\sum_i x_i G(x-x_i)}{\sum_i G(x-x_i)} - x_i \tag{29}$$

Since the gradient is the difference between the mean significant pixels x_i located near x and its current value, the local maximum value is selected through an iterative process. In the case where y_k is the current approximation of the local maximum value, the value is substituted for y_{k+1} during further iterations, considering the expression

$$y_{k+1} = y_k + m(y_k) = \frac{\sum_i x_i G(y_k-x_i)}{\sum_i G(y_k-x_i)} \tag{30}$$

The technique works until the set number of repetitions is reached, or until the displacement value (29) is below the set boundary value. In the process of ordered image splitting, the local maximum values are selected by considering the tension x_r and their specific location $x_s = (x, y)$. Therefore:

$$K(x_i) = k\left(\frac{\|x_r\|^2}{h_r^2}\right) k\left(\frac{\|x_s\|^2}{h_s^2}\right) \tag{31}$$

The initial approximation of the local maximum value y_k occurs for all the significant points of the image. The advantage of this technique is the absence of hypotheses concerning the characteristics and formats of sectors. In addition, the number of sectors is calculated automatically.

Upon completion of the ordered splitting, a further list of characteristics proposed by the technique was computed for each significant point of the image fragment. Accordingly, one segment of the gradient characteristic representing a

significant point covers all its features [30]. The second segment of the gradient characteristic of each significant point expresses the initial spatial information regarding its location, that is, X=(x,y) for any considered fragment $s_i i = 1,\dots,N$ of the split image:

$$L = [P(a(X) = s_1), P(a(X) = s_2), \dots, P(a(X) = s_N)] \quad (32)$$

Here, $a(X)$ is a relation describing the space of significant points in the image from fragment marking.

The probability of matching a significant point $s_i i = 1,\dots,N$ to a fragment is calculated as follows:

$$P(a(X) = s_i) = \begin{cases} 1, a(Y) = s_i, \forall Y \in U(X) \\ 0, \exists Y \in U(X): a(Y) = s_i \\ \frac{1}{\sum s_j}, \exists Y_1: a(Y_1) = s_i \wedge \dots \wedge \exists Y_m: a(Y_m) = s_k \\ , Y_1, \dots, Y_m \in U(X) \end{cases} \quad (33)$$

Since $U(X) = \{Y: |Y - X| \leq R\}$, $U(x)$ is a rounded fragment with a semidiameter R, and its center point corresponds to X. Y is the set of classified significant points.

Equation (33) shows that if the significant point is in the considered fragment, the percentage probability that the significant point corresponds to the object will not depend on the value describing the degree of entering the significant point in the studied fragment.

The classification of significant points concerning the considered image fragments relies on their gradient characteristics, using a technique responsible for learning based on sorters acting as a decision tree [31]. The tree is characterized by $\pi: X \to bool$, where X is the set of characteristics of a given selection, the relationship is expressed as true or false, and each leaf corresponds to an answer Y. Tree creation uses main selections through a general recursive process that splits the initial characteristics into several components (Figure 9) [32].

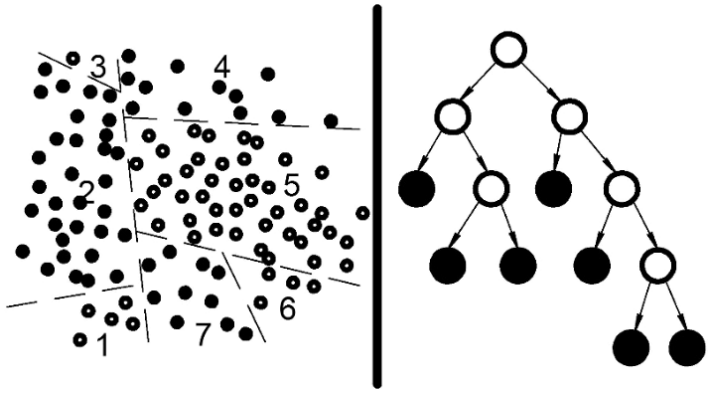

Figure 9. Example of creating decision trees

Several techniques for creating a decision tree are currently available, but the general principle of its creation remains unchanged. Suppose that the selection includes N cases, the characteristics are expressed by M, and the value m is set (as a rule, $m \approx \sqrt{M}$) [33].

Each forest tree is created separately:

- A new selection N is generated based on the training selection. Meanwhile, the components of primary selection can fall into a new selection by repeatedly recurring.
- A tree responsible for classifying the characteristics of the new selections was created. The process of generating new tree nodes considers the characteristics of splitting not from the entire set of M characteristics, but only from t characteristics obtained chaotically. The selection of the optimal t characteristics can proceed according to the different techniques. For example, when using the code proposed by Breiman, the Gini coefficient is applied, which is also the basis for creating the CART.
- A new tree will be created until the generated (described in point 1) selection depletes, resulting in branch cutting.

The ISODATA method, which is currently employed to identify brain lesion foci in images, was utilized to analyze the proposed classification algorithm. The classification of objects proceeds as follows: the forest trees examine a new object that needs classification into a class, voting for the final class for object assignment. Stochastic decision forests are considered optimal techniques for classifying objects. Each technique offers final probability distributions at the output, which is of great importance, in many ways, refining the classification performance through random fields:

$$C = [P(a(X) = s_i), P(a(X) = s_2), \ldots, P(a(X) = s_N)] \quad (34)$$

$$P(a(X) = s_i) = \frac{N_{trees}:a(X)=s_i}{N_{trees}}, i = 1, \ldots, N \quad (35)$$

Here, N_{trees} is the tuning parameter for machine learning. Upon completion of the classification, each significant point will have a gradient describing the probability of matching that significant point to the considered fragment.

The classification of isolated significant points is sometimes associated with the formation of "empty" points, which are most often observed in the outlines of the considered fragments because the sorter does not consider the spatial location of the fragments. In general, the use of Markov fields allows for the significant minimization of this phenomenon. Therefore, selecting the optimal marking lines in the image reduces tension. The one-dimensional component, which expresses the degree of belonging of significant points to some class (the considered fragment), is described as follows:

$$E(x, t) = -log_{10} C \quad (36)$$

where *C* is an arbitrary output of the set of trees from (34).

To find the double component describing the identity of each marked class to neighboring significant points, a technique proposed by Potts is often used:

$$E_{i,j}(t_i, t_j) = 1 - \delta(t_i, t_j) \quad (37)$$

$$\delta(t_i, t_j) = \begin{cases} 1, t_i = t_j \\ 0, t_i \neq t_j \end{cases} \quad (38)$$

The simulation is based on the hypothesis that neighboring significant points may also belong to the same class.

Because the image is split into *k* fragments, the tension reduction process uses *k*-indexed hidden arguments t_j. When *k*>2, achieving this goal can be considered as NP-complex, and creating repetitive steps becomes optimal. This procedure used the α -stretch technique.

The technique is an iterative process in which:

- An approximation is created, and classes are marked with significant points chaotically;
- During each step $\alpha \in 0, \ldots, K-1$, the percentage of the remaining marking lines tends to reduce the tension (a-stretching).
- When the tension reduces, a move to the previous stage or termination occurs.

The tension resulting from a-stretching belongs to the gap:

$$E(T*) \leq E(T) \leq 2kE(T*) \quad (39)$$

Here, *T** represents the optimal value of the hidden argument and *k* represents the contrast of the pairwise tensions.

$$k = \frac{max\, E_{ij}(\beta,\gamma)}{min_{\beta \neq \gamma} E_{ij}(\beta,\gamma)} \quad (40)$$

The maximum reduction in tension affects the classes to which the significant points belong, which should be identical to the optimal groups corresponding to the output of the stochastic forest from the expression. In addition, the maximum tension reduction influences the belonging of neighboring significant points to identical fragments containing the considered object. Finding such an acceptable solution is optimal when analyzing this image.

4. Results

The proposed technique, which makes it possible to separate homogeneous fragments, identifies pathologies on MRI images. The testing process used 270×204 pixels images taken from the Allen Brain Atlas. The technique of splitting images into a set list of fragments was used for ordered fragmentation of a histological section of the mouse brain. Any MRI image series was alternately a trial, whereas the other series were reference images. The study describes the experiments performed in the creation of this technique in detail and a series averaged by many parameters. The developed algorithm was tested using ISODATA clustering. It was decided to use the four clusters as a criterion to stop the function if it stopped changing. A comparison with existing segmentation methods is presented in Table 1, and a comparison of ISODATA with the proposed technique is shown in Figure 10. The criteria used for evaluation were sensitivity, specificity, and the Dice similarity coefficient:

$$Sensitivity = \frac{TP}{TP+TN} \quad (41)$$

$$Specificity = \frac{TN}{TN+FP} \quad (42)$$

$$Dice\ similarity\ coefficient = \frac{2TP}{2TP+FP+FN} \quad (43)$$

Table 1. Comparison of biomedical image segmentation methods

№	Method	Sensitivity	Selectivity	Dice's similarity measure	Reference
1	SparseMultiOCM	0.86	0.99	0.85	Naceur et al. [34]
2	Iterative average	0.76	0.99	0.7	Ellwaa et al. [35]
3	InputCascadeCNN	0.79	0.79	0.79	Havaei et al. [36]
4	U-net	0.9	0.92	0.69	Biratu et al. [37]
5	Region Growing	0.71	0.99	0.8	Biratu et al. [37]
6	Proposed method	0.9	0.88	0.89	

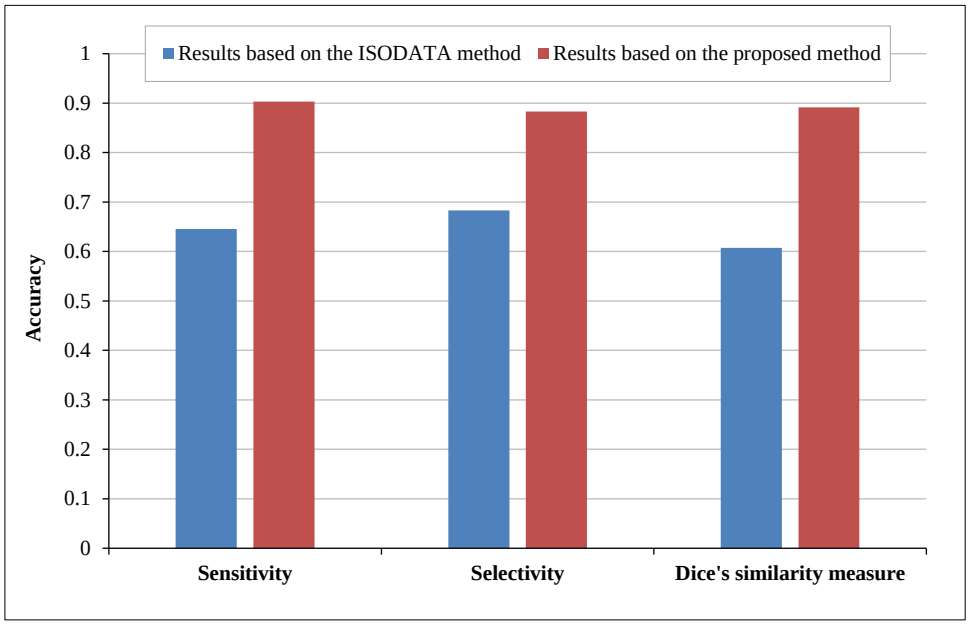

Figure 10. Comparison of ISODATA with the proposed technique

Testing the proposed algorithm showed strong results in identifying individual anatomical structures. The average value over all the structures was 0.86, which exceeded the average accuracy of the existing algorithms by 5-15%.

5. Conclusion

This paper describes new techniques for semantically ordered segmentation and classification of low-dimensionality medical pulses in detail. These techniques rely on the learning process, and their use goes beyond the capabilities of all such techniques, the functioning of which depends on the significant information arrays required for training. The proposed technique saves professionals from the need to mark lines on these arrays. This opens up the possibility of identifying similar objects in images, thereby making it faster and significantly simpler to train the sorter. It is not necessary to identify all significant points belonging to the considered fragment in the image or all outlines of the objects but only to mark which contour lines describing the tension constitute the outline of these objects. The classification of contour lines in the technique for identifying similar objects in images offers the prospect of a reliable separation of objects within one stage. It differs favorably from similar techniques that classify significant points followed by dimensionality-based class grading. The applied characteristics, based on fragments located between contour lines, are very similar to those used by professionals during the visual estimation of objects in the image. The contour lines of the tension dependence can be integrated. Because of the estimation of all closed contour lines, only combined contour lines are typically studied for a single object, thus reducing the possibility of missing an object. In addition, this technique has the advantage of using only the most essential characteristics: the outline of the spectrum of tension and the number of layers required to create contour lines. Splitting images into a set list of fragments can successfully process uneven areas by applying the characteristics of the significant points. The initial processing of the image improves the quality of the test image. The algorithm was tested on brain images; however, it can be used in many biomedical image classification tasks. One potential improvement to the proposed algorithm would be to include additional texture elements in the feature vector, which could facilitate the identification of distinctive features, such as shape and length. This may enhance the ability of the algorithm by adding additional clarifying information that will increase the accuracy of the classification.

6. Declarations

6.1. Author Contributions

Conceptualization, L.Ch. and Y.Y.; methodology, V.K.; software, A.R.; validation, T.A. and A.R.; formal analysis, T.A.; investigation, A.R.; resources, L.Ch.; data curation, V.K.; writing—original draft preparation, T.A.; writing—review and editing, V.K.; visualization, A.R.; supervision, V.K.; project administration, L.Ch. All authors have read and agreed to the published version of the manuscript.

6.2. Data Availability Statement

The data presented in this study are available in the article.

6.3. Funding

Selected findings of this work were obtained under the Grant Agreement in the form of subsidies from the federal budget of the Russian Federation for state support for the establishment and development of world-class scientific centers performing R&D in priority areas of scientific and technological development No. 075-15-2022-307 dated April 20, 2022.

6.4. Institutional Review Board Statement

Not Applicable.

6.5. Informed Consent Statement

Not Applicable.

6.6. Declaration of Competing Interest

The authors declare that there are no conflicts of interest concerning the publication of this manuscript. Furthermore, all ethical considerations, including plagiarism, informed consent, misconduct, data fabrication and/or falsification, double publication and/or submission, and redundancies have been completely observed by the authors.

7. References

[1] Fawzi, A., Achuthan, A., & Belaton, B. (2021). Brain image segmentation in recent years: A narrative review. Brain Sciences, 11(8), 1055. doi:10.3390/brainsci11081055.

[2] Akkus, Z., Galimzianova, A., Hoogi, A., Rubin, D. L., & Erickson, B. J. (2017). Deep Learning for Brain MRI Segmentation: State of the Art and Future Directions. Journal of Digital Imaging, 30(4), 449–459. doi:10.1007/s10278-017-9983-4.

[3] Marchesin, S., Giachelle, F., Marini, N., Atzori, M., Boytcheva, S., Buttafuoco, G., Ciompi, F., Di Nunzio, G. M., Fraggetta, F., Irrera, O., Müller, H., Primov, T., Vatrano, S., & Silvello, G. (2022). Empowering digital pathology applications through explainable knowledge extraction tools. Journal of Pathology Informatics, 13, 100139. doi:10.1016/j.jpi.2022.100139.

[4] Moser, E., Stadlbauer, A., Windischberger, C., Quick, H. H., & Ladd, M. E. (2009). Magnetic resonance imaging methodology. European Journal of Nuclear Medicine and Molecular Imaging, 36(SUPPL. 1), 30–41. doi:10.1007/s00259-008-0938-3.

[5] Chen, J. E., & Glover, G. H. (2015). Functional Magnetic Resonance Imaging Methods. Neuropsychology Review, 25(3), 289–313. doi:10.1007/s11065-015-9294-9.

[6] Budde, M. D., & Frank, J. A. (2012). Examining brain microstructure using structure tensor analysis of histological sections. NeuroImage, 63(1), 1–10. doi:10.1016/j.neuroimage.2012.06.042.

[7] Polezhaev, D. V., Tatarkanov, A. A., & Alexandrov, I. A. (2023). Forming the Architecture of a Multi-Layered Model of Physical Data Storage for Complex Telemedicine Systems. HighTech and Innovation Journal, 4(4), 797–810. doi:10.28991/HIJ-2023-04-04-09.

[8] Giger, M., & MacMahon, H. (1996). Image processing and computer-aided diagnosis. Radiologic Clinics of North America, 34(3), 565–596. doi:10.1016/s0033-8389(22)00492-4.

[9] Bozek, J., Mustra, M., Delac, K., & Grgic, M. (2009). A survey of image processing algorithms in digital mammography. Studies in Computational Intelligence, 231, 631–657. doi:10.1007/978-3-642-02900-4_24.

[10] Ghaheri, A., Shoar, S., Naderan, M., & Hoseini, S. S. (2015). The applications of genetic algorithms in medicine. Oman Medical Journal, 30(6), 406–416. doi:10.5001/omj.2015.82.

[11] Jiao, L., & Zhao, J. (2019). A Survey on the New Generation of Deep Learning in Image Processing. IEEE Access, 7, 172231–172263. doi:10.1109/ACCESS.2019.2956508.

[12] Das, S., & Konar, A. (2009). Automatic image pixel clustering with an improved differential evolution. Applied Soft Computing Journal, 9(1), 226–236. doi:10.1016/j.asoc.2007.12.008.

[13] Yin, H., Varava, A., & Kragic, D. (2021). Modeling, learning, perception, and control methods for deformable object manipulation. Science Robotics, 6(54), eabd8803. doi:10.1126/scirobotics.abd8803.

[14] Borodin, A. A., Kabulova, E. G., & Polozhentsev, K. A. (2016). Video detection of problems in the melting of consumable electrodes in a vacuum arc furnace. Steel in Translation, 46(5), 322–324. doi:10.3103/S0967091216050041.

[15] Zhang, J., Zhong, Y., & Gu, C. (2018). Deformable Models for Surgical Simulation: A Survey. IEEE Reviews in Biomedical Engineering, 11, 143–164. doi:10.1109/RBME.2017.2773521.

[16] Huang, X., Liu, Y., Li, Y., Qi, K., Gao, A., Zheng, B., Liang, D., & Long, X. (2023). Deep Learning-Based Multiclass Brain Tissue Segmentation in Fetal MRIs. Sensors, 23(2), 655. doi:10.3390/s23020655.

[17] Yousaf, F., Iqbal, S., Fatima, N., Kousar, T., & Shafry Mohd Rahim, M. (2023). Multi-class disease detection using deep learning and human brain medical imaging. Biomedical Signal Processing and Control, 85, 104875. doi:10.1016/j.bspc.2023.104875.

[18] Pan, S., Liu, X., Xie, N., & Chong, Y. (2023). EG-TransUNet: a transformer-based U-Net with enhanced and guided models for biomedical image segmentation. BMC Bioinformatics, 24(1), 85. doi:10.1186/s12859-023-05196-1.

[19] Trombini, M., Solarna, D., Moser, G., & Dellepiane, S. (2023). A goal-driven unsupervised image segmentation method combining graph-based processing and Markov random fields. Pattern Recognition, 134, 109082. doi:10.1016/j.patcog.2022.109082.

[20] Fernando, K. R. M., & Tsokos, C. P. (2023). Deep and statistical learning in biomedical imaging: State of the art in 3D MRI brain tumor segmentation. Information Fusion, 92, 450–465. doi:10.1016/j.inffus.2022.12.013.

[21] Qiu, B., Wang, Z., Tang, Z., Chen, C., Fan, Z., & Li, W. (2016). Automated cropping intensity extraction from isolines of wavelet spectra. Computers and Electronics in Agriculture, 125, 1–11. doi:10.1016/j.compag.2016.04.015.

[22] Gembris, D., Taylor, J. G., Schor, S., Frings, W., Suter, D., & Posse, S. (2000). Functional magnetic resonance imaging in real time (FIRE): Sliding- window correlation analysis and reference-vector optimization. Magnetic Resonance in Medicine, 43(2), 259–268. doi:10.1002/(SICI)1522-2594(200002)43:2<259::AID-MRM13>3.0.CO;2-P.

[23] Barmak, A. V., Krak, Y. V., Manziuk, E. A., & Kasianiuk, V. S. (2019). Information technologyof separating hyperplanes synthesisfor linear classifiers. Journal of Automation and Information Sciences, 51(5), 54–64. doi:10.1615/JAutomatInfScien.v51.i5.50.

[24] Schölkopf, B., Mika, S., Burges, C. J. C., Knirsch, P., Müller, K. R., Rätsch, G., & Smola, A. J. (1999). Input space versus feature space in kernel-based methods. IEEE Transactions on Neural Networks, 10(5), 1000–1017. doi:10.1109/72.788641.

[25] Alexandrov, I. A., Kirichek, A. V., Kuklin, V. Z., & Chervyakov, L. M. (2023). Development of an Algorithm for Multicriteria Optimization of Deep Learning Neural Networks. HighTech and Innovation Journal, 4(1), 157–173. doi:10.28991/HIJ-2023-04-01-011.

[26] Petro, A. B., Sbert, C., & Morel, J.-M. (2014). Multiscale Retinex. Image Processing On Line, 4, 71–88. doi:10.5201/ipol.2014.107.

[27] Akbas, E., & Ahuja, N. (2020). Low-level multiscale image segmentation and a benchmark for its evaluation. Computer Vision and Image Understanding, 199, 103026. doi:10.1016/j.cviu.2020.103026.

[28] Veksler, O., Boykov, Y., & Mehrani, P. (2010). Superpixels and supervoxels in an energy optimization framework. Lecture Notes in Computer Science (including subseries Lecture Notes in Artificial Intelligence and Lecture Notes in Bioinformatics): Vol. 6315 LNCS, 211–224. doi:10.1007/978-3-642-15555-0_16.

[29] Ghassabeh, Y. A., & Rudzicz, F. (2018). Modified mean shift algorithm. IET Image Processing, 12(12), 2172–2177. doi:10.1049/iet-ipr.2018.5600.

[30] Bechar, M. E. A., Settouti, N., Barra, V., & Chikh, M. A. (2018). Semi-supervised superpixel classification for medical images segmentation: application to detection of glaucoma disease. Multidimensional Systems and Signal Processing, 29(3), 979–998. doi:10.1007/s11045-017-0483-y.

[31] Xu, G., Liu, M., Jiang, Z., Söffker, D., & Shen, W. (2019). Bearing fault diagnosis method based on deep convolutional neural network and random forest ensemble learning. Sensors (Switzerland), 19(5), 1088. doi:10.3390/s19051088.

[32] Minciullo, L., Bromiley, P. A., Felson, D. T., & Cootes, T. F. (2017). Indecisive trees for classification and prediction of knee osteoarthritis. Lecture Notes in Computer Science (including subseries Lecture Notes in Artificial Intelligence and Lecture Notes in Bioinformatics): Vol. 10541 LNCS, 283–290. Springer. doi:10.1007/978-3-319-67389-9_33.

[33] Thomas, T., P. Vijayaraghavan, A., & Emmanuel, S. (2020). Applications of Decision Trees. Machine Learning Approaches in Cyber Security Analytics, 157–184. doi:10.1007/978-981-15-1706-8_9.

[34] Ben naceur, M., Akil, M., Saouli, R., & Kachouri, R. (2020). Fully automatic brain tumor segmentation with deep learning-based selective attention using overlapping patches and multi-class weighted cross-entropy. Medical Image Analysis, 63, 101692. doi:10.1016/j.media.2020.101692.

[35] Ellwaa, A., Hussein, A., AlNaggar, E., Zidan, M., Zaki, M., Ismail, M. A., & Ghanem, N. M. (2016). Brain tumor segmantation using random forest trained on iteratively selected patients. Lecture Notes in Computer Science (including subseries Lecture Notes in Artificial Intelligence and Lecture Notes in Bioinformatics): Vol. 10154 LNCS, 129–137. Springer. doi:10.1007/978-3-319-55524-9_13.

[36] Havaei, M., Davy, A., Warde-Farley, D., Biard, A., Courville, A., Bengio, Y., Pal, C., Jodoin, P. M., & Larochelle, H. (2017). Brain tumor segmentation with Deep Neural Networks. Medical Image Analysis, 35, 18–31. doi:10.1016/j.media.2016.05.004.

[37] Biratu, E. S., Schwenker, F., Debelee, T. G., Kebede, S. R., Negera, W. G., & Molla, H. T. (2021). Enhanced region growing for brain tumor MR image segmentation. Journal of Imaging, 7(2), 22. doi:10.3390/jimaging7020022.